Real Space Soft X-ray Imaging at 10 nm Spatial Resolution

W. Chao[1], P. Fischer[1], T. Tyliszczak[2], S. Rekawa[1], E. Anderson[1], and P. Naulleau[1]

[1]Center for X-ray Optics, Lawrence Berkeley National Laboratory, Berkeley, CA 94720
[2]Advanced Light Source, Lawrence Berkeley National Laboratory, Berkeley, CA 94720

Using Fresnel zone plates made with our robust nanofabrication processes, we have successfully achieved 10 nm spatial resolution with soft x-ray microscopy. The result, obtained with both a conventional full-field and scanning soft x-ray microscope, marks a significant step forward in extending the microscopy to truly nanoscale studies.

PACS: 68.37.Yz, 42.79.Ci

The scientific interest and technological importance of nanoscale phenomena have triggered the development of a plethora of characterization techniques, including imaging tools with high spatial resolution. Soft x-ray microscopy is of particular interest, since it offers a unique combination of properties, such as the short wavelength of soft x-rays, which allows for nanometer spatial resolution, the elemental specific photoabsorption, and the ultrashort soft x-ray pulses at the upcoming soft x-ray sources such as free electron lasers (FEL). It opens new research avenues in a myriad of fields including material sciences, biology, environmental science, and astrophysics [1]. For example, a spatial resolution to below 10 nm could facilitate investigation of the internal structures of nanoparticles and magnetic vortex cores [2-4], engineering of organic photovoltaic materials [5], and understanding of catalyst chemistry in energy science [6].

Here, we report the achievement of 10nm spatial resolution with soft x-ray microscopy, using both the conventional full-field and scanning imaging technique. To our knowledge, the result is one of the best achieved to date. Although a similar result was demonstrated recently using a novel zone plate design at a scanning transmission soft x-ray microscope (STXM) [7], the result here was obtained with a simpler zone plate fabrication process.

The designs of conventional transmission soft x-ray microscopes (TXM) and STXMs have been described elsewhere [8, 9]. In brief, a conventional TXM condenses x-rays by a large zone plate onto the sample, which in turn is imaged by a "micro" zone plate downstream (Fig 1). An incoherent bend magnet source is used. In an STXM, a zone plate focuses x-rays to a small spot on the sample. The sample is raster scanned by the spot, and the transmitted x-rays are collected by a detector downstream. To obtain a small scanning spot for high spatial resolution, the focusing zone plate is

illuminated by spatially coherent x-rays. The experiments discussed here utilized two x-ray microscopes at the Advanced Light Source (ALS): the full-field transmission microscope, XM-1, at the beamline 6.1.2 [10], and the scanning transmission microscope, MES-STXM, at the beamline 11.0.2 [11].

The spatial resolutions of a TXM and STXM mainly depend on the resolving power of the imaging and focusing zone plates, respectively, and the radiation bandwidth. In general, a Fresnel zone plate's resolving power is determined by its outermost zone width (Δr), zone placement, and the diffraction order used. The diffraction-limited resolution of a zone plate is equal to $\Delta r/m$, where m is the diffraction order. As a zone plate is strongly chromatic, one important requirement for achieving this resolution is to use narrow band radiation; the spectral purity ($\lambda/\Delta\lambda$) needs to be equal or higher than the total number of zones (N) in the zone plate [8], i.e., $\lambda/\Delta\lambda \geq mN$.

Hence, to increase zone plate resolution, narrower zones or operating the lens in higher diffraction order are needed. The latter method is attractive, yet very challenging, as the efficiency of a Fresnel zone plate decreases rapidly with increasing diffraction orders. Furthermore, the required spectral purity is m times that for the first diffraction order. A high brightness source with narrow band illumination would be needed to compensate for the reduced efficiency. This approach was recently demonstrated with an undulator based full-field microscope at BESSY II in Berlin/Germany, where a spatial resolution better than 14 nm was achieved with third diffraction order [12]. For the work presented here, we have chosen to reduce the zone widths to maintain efficiency.

Defining 10-15 nm wide zones in high fidelity was non-trivial. The challenge stemmed from the requirements of zone plate lithographic processes: very high lithographic resolution, high zone placement accuracy, and the need for fabricating smooth, curved structures with slowly varying feature density and modest aspect ratio. To meet these requirements, we developed a robust electron beam overlay lithographic process [13], in which a zone plate pattern is divided into two complementary zone sets, each containing alternating opaque zones. These semi-dense zone sets are fabricated sequentially on the same substrate, and overlaid with accuracy better than $\Delta r/3$. We executed this process using the electron beam lithographic system, the Nanowriter [14], which utilizes a pattern generator optimized for curved structures, and calibration and alignment algorithms developed for sub-pixel placement accuracy. Micro zone plates (MZP) of 12 nm outermost zone width have been successfully fabricated [15] in high yield (~25%) with this process.

A second factor that impacts spatial resolution is imaging coherence. We illustrate this effect by considering the XM-1 full-field microscope. Since the condenser zone plate (CZP) is incoherently illuminated by the bend magnet source, the CZP determines the degree of spatial coherence in the

sample plane, and thus influences image fidelity [16]. Fig 2 shows the simulated image contrasts produced by the XM-1 for different periods of binary, equal line and space objects. The calculations, performed using the commercial PROLITH simulation tool, assume a 12 nm MZP and a wavelength of 1.75 nm (707eV). They further assume an annular CZP with a central stop. The degree of the imaging coherence are described by the partial coherence factor [17], σ (or m [16]), which is equal to the ratio of the numerical apertures of the CZP (NA_{CZP}) and MZP (NA_{MZP}), i.e., $\sigma = NA_{CZP}/NA_{MZP}$. For $NA_{CZP} \ll NA_{MZP}$, σ is zero and the imaging is simply coherent. In this case, the image contrasts match the object contrasts perfectly for large line periods (or small spatial frequencies), until the period is equal to the smallest zone period ($2\Delta r$) of the MZP (Fig 2). No modulation of smaller period gratings can be detected by the microscope. As NA_{CZP} increases, σ increases and the imaging becomes partially coherent. The microscope can image the small period patterns, at the expense of the contrasts at the larger periods. To quantify the increase in the microscope's resolving power as the result of the imaging coherence, the half-periods at which the image contrasts equal to 15.3% for different σ values are compared (Fig. 2). The 15.3% contrast value is chosen to correspond to the Rayleigh criterion [19]. As one can see, the half-period decreases with reduced coherence (larger σ). When NA_{CZP} is equal to NA_{MZP} ($\sigma =1$), the half-period is equal to $0.55\Delta r$, almost half of that in the coherent case. Thus, with partial coherence, set by the appropriate CZP, the microscope can be improved to resolve dense features finer than the smallest zones of MZP. One should note, however, that as partial coherent imaging is a nonlinear process, the optimum σ values depend on the object's optical profiles. By comparing the knife edge and dense grating image profiles for different coherence conditions, Heck, et al. concluded that from the perspective of resolution enhancement, σ between 0.4 and 0.7 is a good compromise for general imaging with full-field microscopes [18].

To exploit the partial coherence effect, we have successfully fabricated CZPs with 30 nm outer zones to match the 12 nm MZPs. They were fabricated using a conventional electron beam lithographic process [14] with a single PMMA resist layer. The CZPs, made in gold, have a diameter of 9.8 mm, and a central stop of 7 mm in diameter. The partial coherence factor made by the CZP and MZP is 0.4. The angle subtended by the central stop is $0.28NA_{MZP}$. We installed both optics on the XM-1, and tested the resolution performance of the system with our standard Mo/Si multilayer test objects. These objects, made with magnetron sputtering, have layer thickness accuracy of 1-2 atoms. In preparation for viewing edge on in transmission, their cross sections were thinned and exposed using a commercial focused ion beam technique. Due to the modest spectral resolution provided by the CZP and the pinhole, the MZP is limited to have 500 zones. This design constraint, combined with the 12 nm zone width (Fig 1), yields a

rather short working distance in the soft x-ray region (e.g., 164 µm at 1.75 nm wavelength). To use the MZP, the zone plate and sample were mounted in a modified design [19] of the sample stage.

Fig 3(a) shows a flattened x-ray image of a multilayer test object, which has line patterns with half-periods of 9 nm, 10 nm, and 11 nm. As one can see, the image clearly shows the lines and spaces in both the 10 nm and 11 nm half-period patterns. At 9 nm half-period, no modulation is observed. The resolved features are smaller than 12 nm, the smallest zone width of the MZP. This result is consistent with the resolution enhancement by the condenser illumination discussed earlier. The transmission electron microscopy image of the same object is shown in Fig 3(b) for comparison. To our best knowledge, the resulting x-ray image demonstrates the highest resolution achieved with soft x-ray full-field microscopy.

The absolute contrasts measured at the three periods in the x-ray image, as well as those at larger periods (not shown), are plotted in Fig. 3(c). These contrasts were obtained by averaging the intensity profiles along the lines, and calculating the values according to the formula, (Imax – Imin)/(Imax + Imin). In this formula, Imax and Imin are the average intensities of the peaks and troughs in the profiles. Fig 3(c) also shows the predicted image contrasts of the Mo/Si test objects used in the experiment. These calculations, made with PROLITH, assume the best estimated object thickness of 160 nm. One can see in Fig 3(c) that the measured contrasts are significantly lower than the calculated ones. One potential cause is the residual vibration in the sample stage, which could smear the modulations. Another cause may be the presence of stray light in the images. In the microscope setup, the pinhole was 8 µm in diameter, slightly larger than the ideal size, and could introduce unfocused light to the CCD detector. To estimate the stray light dependence on the pinhole size, ray tracing analysis of a simple imaging system containing a CZP, a pinhole, and an MZP was performed. The first diffraction order was considered for the condenser, and up to the third diffraction order was considered for the MZP. A small band of radiation centered at 1.75 nm wavelength was also assumed. The analysis concluded that an 8 µm diameter pinhole can lead to stray light through the second diffraction order of the MZP, with intensity approximately equal to 10% of that of the focused light.

To further verify the effect of imaging coherence on resolution, we performed imaging tests at the MES-STXM system. This microscope uses an undulator, a grating monochromator, and a spatial filter to produce narrow band, nearly spatially coherent x-rays on the focusing zone plate (FZP). Under this condition, the MES-STXM by reciprocity [20] is equivalent to a full-field microscope that has an imaging lens identical to the FZP and a condenser having the same pupil properties as the detector. By this equivalence, the partial coherence factor of the MES-STXM is equal to the ratio of the numerical aperture subtended by the detector at the sample ($NA_{detector}$) to that of the FZP (NA_{FZP}). Since $NA_{detector}$ is

about 2.5 times NA_{FZP}, σ is equal to 2.5, and the microscope behaves almost like an incoherent system. With a diffraction-limited focusing zone plate and infinite signal to noise, the microscope could theoretically detect line patterns with periods down to half of the smallest zone period in the focusing lens. We tested the microscope with a 17 nm outermost zone width FZP, fabricated using a similar zone plate process used for the 30 nm CZPs. We did not choose the 12 nm MZPs, due to their short focal length and lack of the required central stops. The 17 nm FZP has 1700 zones, 50 µm diameter central stop, and a focal length of 1135 µm at 1.77 nm wavelength (700eV). Fig 4 (a) shows the x-ray images of the same Mo/Si multilayer test patterns used in the XM-1 testing above, with a half-period of 9 nm, 10 nm, and 11 nm. During the experiment, a relative vibration between the sample and zone plate stages of approximately ± 2.5 nm (2 st dev.) was detected by the interferometer. As one can see in Fig 4(a), clear modulations were produced by the microscope for the 10 nm and 11 nm patterns. For the 9 nm pattern, faint, noisy lines can be discerned. As the theoretical half-period for zero modulation is 8.5 nm, the minute modulation observed in the 9 nm pattern image indicates that the MES-STXM with the 17 nm zone plate performed close to its theoretical limit. Fig 4(b) summarizes the image contrasts measured from the three x-ray images.

For better understanding of the observed image fidelity, we employed PROLITH to calculate the expected contrasts under the experimental conditions. The calculation assumed a Gaussian vibration profile with a standard deviation equal to 1.25 nm. The calculation results are also shown in Fig 4(b). As one would expect, the contrast decreases "linearly" with the spatial frequency of the Mo/Si test object, and reaches zero at a frequency equivalent to 8.5 nm half-period. The theoretical contrast values for 9 nm, 10 nm, and 11 nm are 1%, 6%, 13%, respectively. In comparison, the x-ray images have measured contrasts of 0.3%, 2.6%, and 3.6% for the same pattern periods. The measurements have significantly lower values. The cause of this is unclear and warrants further investigation.

In conclusion, 10 nm resolution has been successfully achieved with both soft x-ray full-field and scanning microscopy. The result, obtained with the conventional zone plate and microscope designs, is readily extendible to soft x-ray microscopes in synchrotron facilities worldwide. The achievement also marks a significant milestone in the quest of single-digit nanometer resolution with soft x-rays. With the continuing advancement of the overlay and other zone plate fabrication processes [15, 21-23], as well as new microscope development [12], studying nanoscale phenomena at sub-10 nm resolution with soft x-rays generated by not only 3rd generation light sources, but also by x-ray lasers[24] and perhaps table-top sources[25], could come true in the near future.

Acknowledgements

References

[1]   C. David *et al.*, *9th International Conference on X-ray Microscopy* (IOP Publishing, 2009), **186**.
[2]   A. B. Butenko *et al.*, Phys. Rev. B **80**, 134410 (2009).
[3]   E. V. Shevchenko *et al.*, Nature **439**, 55 (2006).
[4]   S. Park *et al.*, Science **323**, 1030 (2009).
[5]   H. Ade, and A. P. Hitchcock, Polymer **49**, 643 (2008).
[6]   E. de Smit *et al.*, Nature **456**, 222 (2008).
[7]   J. Vila-Comamala *et al.*, Ultramicroscopy **109**, 1360 (2009).
[8]   D. T. Attwood, *Soft x-rays and extreme ultraviolet radiation: principles and applications* (Cambridge University Press, Cambridge, U.K., 2000), pp361-363, 365-368.
[9]   M. Howells *et al.*, in *Science of Microscopy*, edited by P. W. Hawkes, and J. C. H. Spence (Springer, New York, 2007), pp 867-868, 870-873.
[10]   P. Fischer, in *Mater. Today* (2010), p. 14.
[11]   T. Tyliszczak *et al.*, AIP Conf. Proc. **705**, 1356 (2004).
[12]   S. Rehbein *et al.*, Phys. Rev. Lett. **103**, 110801 (2009).
[13]   W. Chao *et al.*, Nature **435**, 1210 (2005).
[14]   E. Anderson *et al.*, J. Vac. Sci. Technol. B **18**, 2970 (2000).
[15]   W. Chao *et al.*, J. Vac. Sci. Technol. B **27**, 2606 (2009).
[16]   M. Born, and E. Wolf, *Principles of optics: electromagnetic theory of propagation, interference and diffraction of light* (Cambridge University Press, New York, 1999), pp 595-597
[17]   W. Chao, Ph.D. thesis, University of California, Berkeley, 2005.
[18]   J. M. Heck *et al.*, Journal of X-Ray Science & Technology **8**, 95 (1998).
[19]   W. Chao *et al.*, Opt. Express **17**, 17669 (2009).
[20]   M. E. Barnett, Optik **38**, 585 (1973).
[21]   S. Rehbein, and G. Schneider, in *Proc. 8th Int. Conf. X-ray Microscopy* (Institute of Pure and Applied Physics, 2006), p. 103.
[22]   K. Jefimovs *et al.*, Phys. Rev. Lett. **99**, 264801 (2007).
[23]   J. Reinspach *et al.*, J. Vac. Sci. Technol. B **29**, 011012 (2011).
[24]   P. Emma *et al.*, Nat. Photon. **4**, 641 (2010).
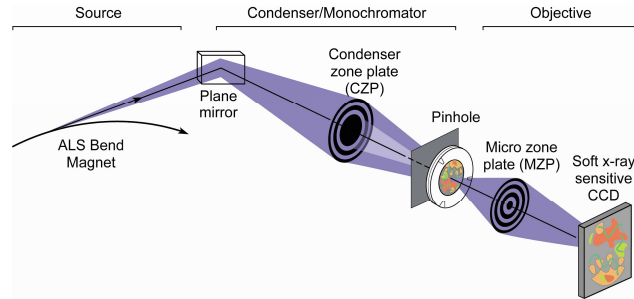[25]   P. A. C. Takman *et al.*, J. Microsc **226**, 175 (2007).

Fig. 1 A schematic of the conventional full-field transmission soft x-ray microscope, XM-1, at the Advanced Light Source (ALS). The CZP, pinhole, and plane mirror serve as a monochromator, providing a modest bandwidth.
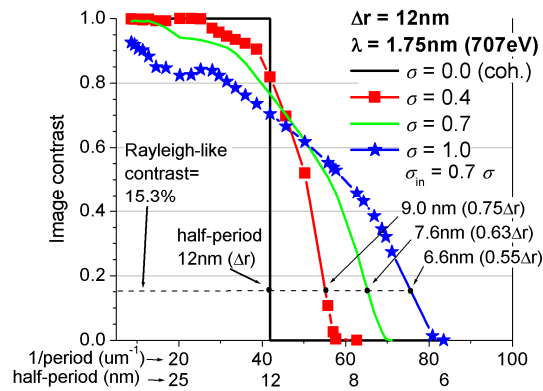

Fig. 2 The simulated image contrasts of different periods of binary, equal line and space patterns, produced by the XM-1 microscope under various degrees of imaging coherence, σ.
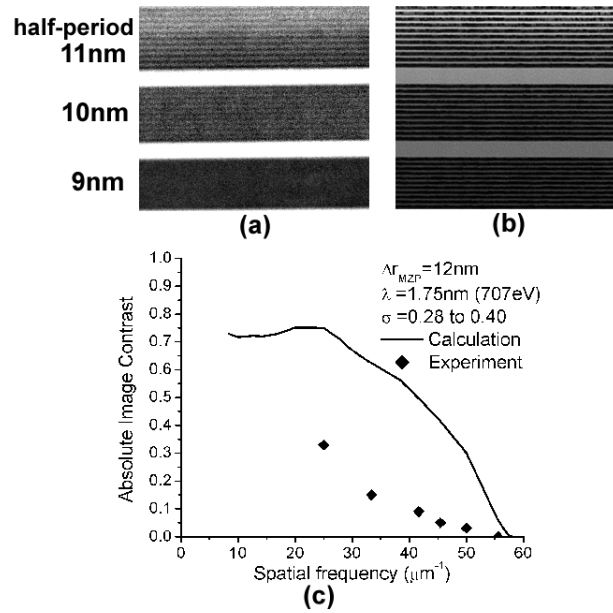
Fig. 3 (a) An x-ray image and (b) a transmission electron image of our standard Mo/Si multilayer test object. The flattened x-ray image was obtained with a 6 sec exposure at 1.75 nm wavelength using the XM-1 microscope. (c) The absolute image contrasts measured at the three periods in (a), as well as those at larger periods, plotted as dots against the spatial frequency of the patterns. The solid line indicates the predicted contrasts.
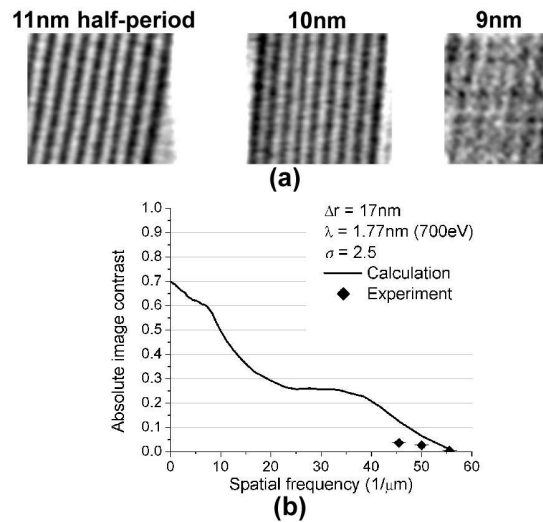
Fig. 4 (a) An x-ray image of the Mo/Si multilayer test object taken by the MES-STXM microscope at 1.77 nm wavelength and with a 2.5 nm step size. The 9 nm pattern image was acquired with 80 ms dwell time (8.5 min exposure), while the 10 nm and 11 nm images were taken with 20 ms dwell time (2.1 min exposure). (b) The absolute image contrasts measured from the images in (a), as well as the predicted contrasts.

DISCLAIMER